Clim Dyn (2011) 37:1643–1660
DOI 10.1007/s00382-010-0937-5

# A transitioning Arctic surface energy budget: the impacts of solar zenith angle, surface albedo and cloud radiative forcing

**Joseph Sedlar · Michael Tjernström · Thorsten Mauritsen · Matthew D. Shupe · Ian M. Brooks · P. Ola G. Persson · Cathryn E. Birch · Caroline Leck · Anders Sirevaag · Marcel Nicolaus**

Received: 25 February 2010 / Accepted: 15 October 2010 / Published online: 4 November 2010


**Abstract** Snow surface and sea-ice energy budgets were measured near 87.5°N during the Arctic Summer Cloud Ocean Study (ASCOS), from August to early September 2008. Surface temperature indicated four distinct temperature regimes, characterized by varying cloud, thermodynamic and solar properties. An initial warm, melt-season regime was interrupted by a 3-day cold regime where temperatures dropped from near zero to −7°C. Subsequently mean energy budget residuals remained small and near zero for 1 week until once again temperatures dropped rapidly and the energy budget residuals became negative. Energy budget transitions were dominated by the net radiative fluxes, largely controlled by the cloudiness. Variable heat, moisture and cloud distributions were associated with changing air-masses. Surface cloud radiative forcing, the net radiative effect of clouds on the surface relative to clear skies, is estimated. Shortwave cloud forcing ranged between −50 W $m^{-2}$ and zero and varied significantly with surface albedo, solar zenith angle and cloud liquid water. Longwave cloud forcing was larger and generally ranged between 65 and 85 W $m^{-2}$, except when the cloud fraction was tenuous or contained little liquid water; thus the net effect of the clouds was to warm the surface. Both cold periods occurred under tenuous, or altogether absent, low-level clouds containing little liquid water, effectively reducing the cloud greenhouse effect. Freeze-up progression was enhanced by a combination of increasing solar zenith angles and surface albedo, while inhibited by a large, positive surface cloud forcing until a new air-mass with considerably less cloudiness advected over the experiment area.

**Keywords** Arctic · Sea ice · Surface energy budget · Cloud radiative forcing · Shortwave radiation · Longwave radiation

J. Sedlar (✉) · M. Tjernström · C. Leck
Department of Meteorology,
Stockholm University, Stockholm, Sweden
e-mail: josephs@misu.su.se

T. Mauritsen
Max Planck Institute for Meteorology, Hamburg, Germany

M. D. Shupe · P. O. G. Persson
University of Colorado and NOAA-ESRL-PSD,
Boulder, CO, USA

I. M. Brooks · C. E. Birch
School of Earth and Environment, University of Leeds,
Leeds, UK

A. Sirevaag
University of Bergen and Bjerknes Center for Climate Research,
Bergen, Norway

M. Nicolaus
Norwegian Polar Institute, Tromsø, Norway

M. Nicolaus
Alfred Wegener Institute for Polar and Marine Research,
Bremerhaven, Germany

## 1 Introduction

The Arctic has become a focal point for studying the Earth's response to a changing climate (e.g. ACIA 2005; Overland et al. 2008; Overland 2009), as it has witnessed amplified surface warming by roughly a factor of two compared to the global average (ACIA 2005; IPCC 2007), as well as warming aloft (Graversen et al. 2008). A central focus is on the reduction of the perennial sea-ice (e.g. Lindsay and Zhang 2005; Serreze et al. 2007; Overland 2009), especially since the record ice-loss of 2007 (e.g. Kay et al. 2008; Zhang et al.

2008a; Lindsay et al. 2009). The debate over the primary forcings responsible for Arctic climate changes is reflected in the literature: changes in the large-scale atmospheric circulation patterns (eg. Graversen 2006; Graversen et al. 2008; Overland et al 2008; Zhang et al. 2008b); radiative forcing due to changes in greenhouse gases (Serreze et al. 2007; Graversen and Wang 2009); inflow of warm ocean water (e.g. Shimada 2006; Polyakov et al. 2007) or a mixture of these causes. The climate change signal is amplified by feedbacks to the system associated with these forcings, such as the ice-albedo feedback (Perovich et al. 2008) and altered cloud-radiative characteristics (Liu et al. 2008; Kay et al. 2008; Kay and Gettelman 2009). Climate forcings and feedbacks thus inherently influence the energy balances at the snow surface and within the sea ice.

The surface energy budget is maintained by radiation and turbulent heat transport, upward turbulent ocean heat transport, conduction of heat and transmission/absorption of shortwave radiation within the snow and ice. The timing of sea-ice transitions occurring both in spring and autumn are modulated by the evolution of these processes. As the melt season transitions to freeze-up, sources of heat and moisture to the atmospheric boundary layer (ABL) decrease as open leads and melt ponds freeze over. Radiative fluxes, and the effect of cloud cover, also change seasonally and spatially in the Arctic. The cloud greenhouse warming effect typically dominates over the cloud reflectivity cooling effect across much of the Arctic, however the relative magnitudes of these are dependent on solar zenith angle (SZA), surface albedo and cloud microphysical properties (Curry et al 1996; Walsh and Chapman 1998; Intrieri et al. 2002a; Shupe and Intrieri 2004).

In recent years, sea-ice extent has been readily observed by satellite. Direct, detailed observational data of the surface energy balance and the effects of clouds over the central Arctic Ocean are required to understand the complexity of ongoing processes. Observational data are often confined to intermittent experimental campaigns, although the knowledge gained from such experiments is invaluable (Ruffieux et al. 1995; Nilsson et al. 2001; Persson et al. 2002; Birch et al. 2009). Measurements of physical processes such as turbulent heat fluxes, clouds and cloud-radiative interactions and the extent of the ice-albedo feedback are needed for process-oriented studies and to enhance the understanding of Arctic climate. Such physical processes govern the interactions among the sea ice, the ABL and the free troposphere (e.g. Curry et al. 1996). Parameterizations of these processes for numerical modeling should be validated against observational data from the central Arctic. However, due to the paucity of such data, the parameterizations tend to rely on lower-latitude observations for development and validation (Tjernström et al. 2005), highlighting the importance of such data.

Cloud climatologies over the central Arctic Ocean generally show a maximum frequency of occurrence during the sunlit months (e.g. Curry et al. 1996; Intrieri et al. 2002b). The presence of cloud cover influences both the short- and longwave-radiative fluxes at the surface, and the presence of a highly reflective surface during times of low sun angles leads to a complex cloud-radiative interaction in the Arctic (Curry et al. 1996). In this paper, we examine observations taken during the final stages of the 2008 sea-ice melt season from the Arctic Summer Cloud Ocean Study (ASCOS). We measured all energy fluxes at the snow surface and below the sea ice, and examine the snow surface and ice energy budgets from mid-August until early September. The timing of ASCOS allows a detailed investigation into the processes and physical constraints related to, and forcing, the energy budget transitions in an Arctic high-latitude environment. We first provide a description of the instrumentation and methods used to calculate the energy budgets and cloud radiative forcing. The progression of the surface response to cloud radiative forcing is examined in detail, focusing on the dominant factors of importance for both short- and longwave radiative forcing. The paper closes with a discussion and conclusions drawn from the main results.

## 2 Experiment and data

ASCOS contributed to the International Polar Year 2007–2009. The primary objective was to understand the processes leading to the formation and life-cycle of low-level clouds and the role they play in the surface energy budget of the high Arctic during the late summer to early fall transition. ASCOS was interdisciplinary, with science teams focused on meteorology, physical oceanography, atmospheric gas-phase chemistry, aerosol chemistry and physics, and marine biology. It was the fourth, and largest, in a series of central-Arctic experiments which occurred during 1991 (Leck et al. 1996), 1996 (Leck et al. 2001) and 2001 (Leck et al. 2004; Tjernström et al. 2004). Like its predecessors, ASCOS was conducted onboard the Swedish icebreaker Oden. Oden left Svalbard on 2nd August, returning on 9 September 2008. By 12th August, after a few brief open water and marginal ice zone research stations, Oden moored and drifted with a 3 × 6 ice floe for nearly 21 days. The expedition track, from about N87°21′ W01°29′ to N87°09′ W11°01′, is illustrated in Fig. 1.

A detailed description of ASCOS including the instrumentation and measurements is found in Tjernström et al. (in prep.). Onboard instrumentation used in this study includes a suite of ship-based remote-sensing instruments: a millimeter cloud radar (MMCR; Moran et al. 1998), two ceilometer and visibility sensors and a dual wavelength

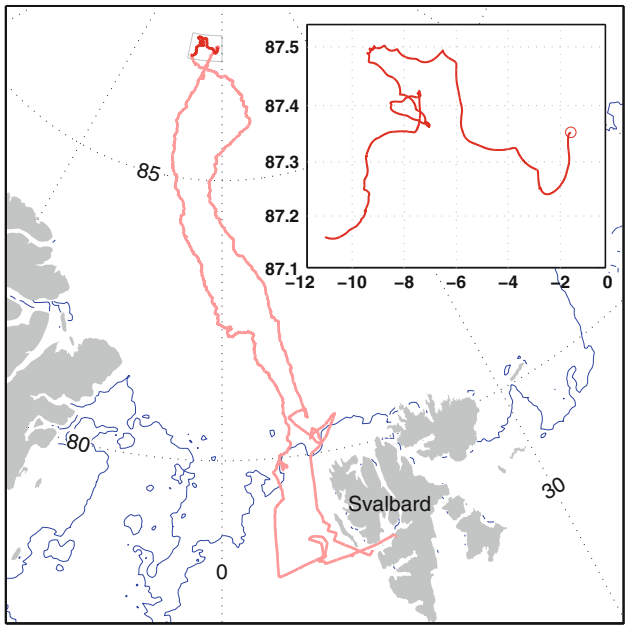


**Fig. 1** Cruise track for ASCOS (*light red*) and ice drift track (*dark red*); insert zooms in on the ice drift (latitude vs. longitude, *red ring* indicates start position). The *blue line* indicates the approximate southern ice edge as of 12 August 2008

(24/31 GHz) microwave radiometer (MWR) (Westwater et al. 2001). The MMCR provides information on the reflectivity of cloud and precipitation particles. Its lowest range gate is at 105 m; clouds and fog below this height are not sensed. The theoretical minimum detectable signal is around −55 dBZ in the lowest few hundred meters, therefore only very low concentrations of small droplets may not be detected. The MWR provides vertically integrated cloud liquid water path (LWP), employing a statistical bi-linear retrieval resulting in a 25 g $m^{-2}$ uncertainty (Westwater et al. 2001). This uncertainty includes instrument and calibration biases, which at times lead to a drifting baseline value. Thus, occasional negative LWPs within the uncertainty range are observed. All remote-sensing instruments were operated continuously with very high data recovery. Six-hourly radiosonde profiles were also part of the continually operated onboard measurements.

During the ice drift, a row of masts and instruments were aligned on the ice extending away from the ship to minimize both ship and instrument interference. Two masts, 15 and 30 m, were instrumented for micrometeorological measurements. The 15 m mast supported five levels of turbulence measurements from 0.94 to 15.4 m, along with aspirated sensors for profile measurements of mean temperature and humidity. The 30 m mast supported a single sonic anemometer. Sensible heat fluxes are available at all six flux-measurement levels, while latent heat fluxes from open-path gas analyzers were at 3.2 and 15.4 m. Turbulent heat fluxes were derived using eddy covariance techniques, with the wind measurements rotated into a consistent streamline-oriented coordinate system using the planar-fit method (Wilczak et al. 2001). Data recovery for surface energy budget calculations was quite good, around 80% for sensible and latent heat fluxes. The primary data loss occurred when cold and humid conditions resulted in rime formation on the instruments, primarily during day of year (DoY) 234–236 and 243–245. Turbulent flux uncertainties are difficult to estimate but at least on the order of 10% (Andreas et al. 2005). Raw data time series were checked and flagged for data quality prior to flux calculations.

Eight thermocouples measuring surface temperature and four thermocouples measuring in-ice temperature were deployed in the vicinity of four broadband radiometers. All themocouples were covered with white heat-shrink wrapping to minimize shortwave heating. Precision Solar Pyranometers (PSP) and Precision Infrared Radiometers (PIR) measuring down- and upwelling shortwave and longwave radiation were installed approximately 1.5 m above an undisturbed snow surface. Initially, two melt ponds were located within approximately 30 m from the radiometers but within the field of view of the instruments. These melt ponds gradually froze over and became covered with snow and rime during the deployment. The radiometers were calibrated against reference radiometers prior to deployment. The factory-specified uncertainty for the PSPs are approximately 3% of incident shortwave radiation for zenith angles encountered during ASCOS, which is equivalent to 3 W $m^{-2}$ based on median observations. The uncertainty is approximately 4 W $m^{-2}$ for the longwave PIR measurements. The radiometers were prone to icing during DoYs 234–236 and 243–245. The PIRs, with a darker dome, were considerably less iced than the PSPs, especially the upward-looking PSP. The surface temperatures were compared to the radiative surface temperature from the downward-facing PIR using a surface emissivity of 0.99 (cf. Persson et al. 2002) revealing a good correspondence throughout the deployment, with an average difference of 0.2 ± 1°C standard deviation. Also deployed on the ice was a phased-array sodar system, observing the acoustic backscatter profiles associated with temperature variance up to ~500 m. Two self-calibrating heat flux plates were buried approximately 0.05 m below the initial snow surface to measure the near-surface conductive heat flux. The upper faces of the plates were painted white to minimize absorption of shortwave radiation penetrating the upper snow cover. The uncertainty of these instruments varied as the depth below the snow surface changed with melting, freezing and precipitation, but the absolute RMSE from the mean during the campaign was approximately 0.6 W $m^{-2}$.

An ocean-observation site contained shortwave radiation sensors above and below approximately 1.8 m thick sea ice, as well as under-ice eddy correlation instruments for measurements of oceanic turbulent fluxes. The shortwave radiation measurements are based on three spectral radiometers spanning wavelengths from 320 to 950 nm with a spectral resolution of 3.3 nm, hence these instruments do not cover the full shortwave spectrum. Two spectral radiometers measure up- and downwelling radiation at the ice surface and one measures radiation transmitted through the sea ice (Nicolaus et al. 2010). The under-ice turbulence measurements were obtained using so-called Turbulence Instrument Clusters (TICs) which comprise sensors for measuring 3-D velocity, temperature and conductivity (McPhee 2008). TICs were positioned at several levels on a rigid mast which was deployed through the ice and spanned the upper 10 m of the ocean boundary layer. In this study, measurements from the uppermost TIC at 2 m below the ice/ocean interface are used. Current velocities are rotated into a streamline coordinate system and the covariance of vertical deviatory velocity and temperature provide ocean turbulent fluxes (Sirevaag and Fer 2009). The uncertainty in ocean heat flux measurements is on the order of 1 W $m^{-2}$, however, as with the atmospheric turbulent fluxes, the variability within a given time period is often larger than the uncertainty.

The majority of on-ice instruments were operational from mid-day on 13 August; all turbulent flux measurements were operational by the 15th. Formation of rime on instruments was a problem primarily during DoYs 234–236 and 243–245. A careful record of the presence of rime and when it was removed was kept by the on-ice science crew. This record has later been used together with other criteria to screen and correct data in post-processing and data quality assurance. All measurement analysis is based on 10-min averaged variables unless noted otherwise.

## 3 Methods

An energy budget consists of all the components of energy into or out of a system, and the net budget, also referred to as the residual, identifies its respondent sensible and/or latent heating. Conventional energy budget calculations for land surfaces inherently assume the surface to be an infinitesimally thin layer. This is adequate since all shortwave radiation is typically absorbed within a thin layer near the surface. However, snow and sea ice are semi-transparent to shortwave radiation (Perovich 2005). The definition of the surface energy budget adopted for this study is:

$$Q_{\mathrm{sfc}} = R_{\mathrm{s}} + R_{\mathrm{l}} - H_{\mathrm{s}} - H_{\mathrm{l}} + C \quad (1)$$

similar to Intrieri et al. (2002a). $Q_{\mathrm{sfc}}$ is the residual flux, $R$ represents the net radiative fluxes, with subscripts s and l corresponding to short- and long-wave, respectively. $H_{\mathrm{s}}$ and $H_{\mathrm{l}}$ are the turbulent sensible and latent heat fluxes, while $C$ is the conduction of heat to the snow surface from the ice. Flux signs are defined according to their effect on the surface, positive when heating and negative when cooling, except for the turbulent fluxes that are defined traditionally upward such that positive corresponds to a cooling of the surface. In calculating this budget we have assumed that shortwave radiation does not penetrate through the snow, an assumption the authors know to be inaccurate. However, we choose to include this uncertainty rather than making an unsubstantiated guess at the shortwave transmission through the snow layer. Thus, our estimated surface residual will contain a positive, warm bias since we assume net shortwave radiation to be the actual forcing at the surface. Sensitivity tests with reasonable assumptions on shortwave radiation penetration (see Perovich 2005) indicated that although this assumption slightly affects the magnitude of the budget residual, it does not greatly alter the residual trends.

The energy budget for the ice, here defined as the entire slab of ice including the snow layer, is defined as:

$$Q_{\mathrm{ice}} = R_{\mathrm{s}} - R_{\mathrm{sdo}} + R_{\mathrm{l}} - H_{\mathrm{s}} - H_{\mathrm{l}} + H_{\mathrm{o}} \quad (2)$$

where $R_{\mathrm{sdo}}$ is the downward shortwave radiation transmitted through the ice into the upper ocean, and $H_{\mathrm{o}}$ is the turbulent heat flux from the upper ocean to the ice. Here the heat conduction near the top of the ice is excluded as it merely acts to redistribute heat. The transmission of shortwave radiation to the ocean is sensitive to snow and ice thickness, neither of which were recorded in detail during the ice drift although ice thickness varied at least between 1.5 and 5 m.

Clouds influence the amount of radiation reaching the surface through scattering, reflecting and absorbing/emission of short- and long-wave radiation (e.g. Stephens 1978). Surface cloud radiative forcing (CRF) can be thought of as the effect clouds have on the surface radiation budget. CRF can be quantified by comparing the surface radiative fluxes under cloudy skies with the radiative fluxes under identical, but clear skies (Schneider 1972; Ramanathan et al. 1989):

$$\mathrm{SWF} = R_{\mathrm{s}}(\mathrm{AS}) - R_{\mathrm{s}}(\mathrm{CS}) \quad (3)$$

$$\mathrm{LWF} = R_{\mathrm{l}}(\mathrm{AS}) - R_{\mathrm{l}}(\mathrm{CS}) \quad (4)$$

$$\mathrm{CRF} = \mathrm{SWF} + \mathrm{LWF} \quad (5)$$

where SWF and LWF are short- and longwave forcing, respectively. $R_{\mathrm{s}}$ and $R_{\mathrm{l}}$ are net radiative fluxes for all-sky (AS) and clear-sky (CS) conditions. Positive CRF indicates an enhanced radiative flux warming the surface with the presence of clouds. Note the definition of CRF in Eq. 5 does not include effects on the turbulent heat fluxes at the surface such as in Intrieri et al. (2002a). In this paper, we are only concerned with isolating the instantaneous surface

CRF component, although we are aware that changes in the radiative forcing will manifest changes in the remaining energy budget components.

Clear-sky radiative fluxes were computed using the Fu–Liou delta-four-stream approximation, correlated-k radiative transfer model (Liou et al. 1988; Fu and Liou 1992; Liou 1992). The model requires location, surface albedo, surface emissivity (assumed unity), well-mixed greenhouse gas concentrations and thermodynamic and ozone profiles as inputs. No background aerosol profile was used. Thermodynamic profiles were interpolated to every hour from the radiosondes, resulting in 421 hourly CRF calculations.

Only eight cases were identified as clear-sky cases from the vertically pointing remote sensing suite. Using Eqs. 3 and 4, the mean biases of SWF and LWF during these cases are 13 and $-4$ W m$^{-2}$, respectively. The LWF bias can be explained by the hemispheric view of the instruments, allowing clouds that were not detected by the fields-of-view of the vertically pointing remote sensors to alter the observed fluxes. The upward-looking PSP was prone to significant icing for approximately 20% of the hourly CRF calculations, coinciding with most of the clear-sky cases; the downward-facing PSP remained considerably more ice-free, although not entirely ice-free. Therefore, during times of icing, surface albedo was linearly interpolated in time between radiometer cleanings, and the downward-facing PSP was used to estimate the downwelling shortwave irradiance. Thus, the clear-sky SWF is likely biased high since the downward-facing PSP was not perfectly clean, and corrections to downward shortwave will reflect this error. The SWF bias should be lower during times when icing was not an issue. Thus, since the computed biases of SWF and LWF are believed to be an upper limit, and that instrument icing was not a problem for approximately 80% of the forcing calculations, we estimate the total uncertainty in CRF to be on the order of 10–15 W m$^{-2}$.

Finally, 5-day back trajectories were calculated from the Global Environmental Research online METEX application to estimate the Lagrangian air-mass trajectories towards Oden. The trajectories are 3-D using the 3-D wind field calculated using reanalysis data from the National Centers for Environmental Prediction (Zeng et al. 2008). These were computed using Oden's geographic location during the ice drift, arriving at 200 m above the ship's location. The 200 m level was chosen as representative of the boundary-layer flow but still away from the surface to avoid trajectory correction when a parcel contacts the underlying surface.

## 4 Surface and background atmosphere

Surface and near-surface air temperatures experienced substantial variability, while closely following one another during the ice drift (Fig. 2). The mean air temperature generally followed the mean surface temperature minus twice the standard deviation among the multiple sensors, such that the mean air temperature was approximately equal to or colder than the underlying surface, except for a few occasions when the surface was cooler than the air. Therefore, near-neutral to weakly unstable near-surface stratification was commonly observed, in good agreement with the measured sensible heat fluxes. Often the Arctic is associated with strong static stability, however we find a more neutral surface layer during August. Dashed vertical lines indicate approximate transitions between four distinct surface temperature regimes. Temperature maxima during the 1st and 3rd regimes generally remained near the freezing point of fresh (0°C) and saline water (−1.8°C), respectively. The 2nd and 4th regimes were characterized by significant temperature decreases, down to −7°C during the 2nd regime and approaching −14°C on DoY 245. These regimes are chosen based on common temperature trends in chronological order.

Cloud radar-reflectivity profiles, which are proportional to the particle size to the sixth power, are used to identify vertical locations of cloud and precipitation hydrometeors (Fig. 3). Multiple cloud layers, some being geometrically thick, precipitating systems, were observed during the first regime from DoY 226 through 233 (Fig. 3, top panel). The temperature drop in the 2nd regime (roughly DoY 234–236.5) coincided with weaker reflectivities and tenuous cloud cover that, by the end of DoY 234, temporarily dissipated near the surface. Ceilometers confirmed that the

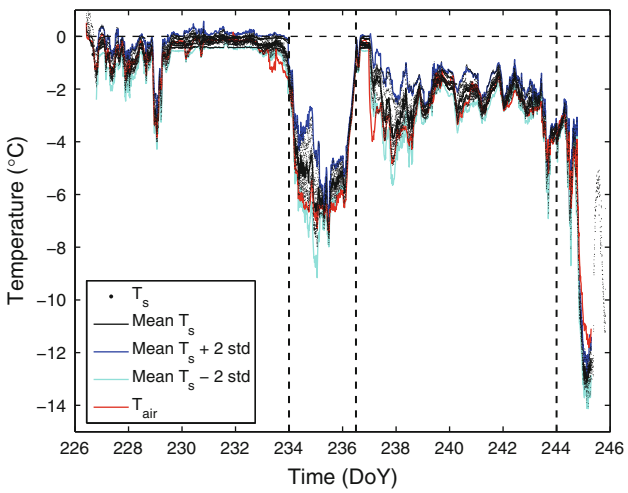


**Fig. 2** Mean air temperature at approximately 1 m a.g.l. (*red*) and surface temperatures from eight different sensors (*black dots*) in °C, as a function of time (*DoY* day of the year). The *solid black line* shows the 10-min averaged surface temperature along with the corresponding plus (*blue*) and minus (*cyan*) twice standard deviations across all eight sensors. *Dashed vertical lines* differentiate between four temperature regimes (see *text*). DoY 226 is 13 August 2008

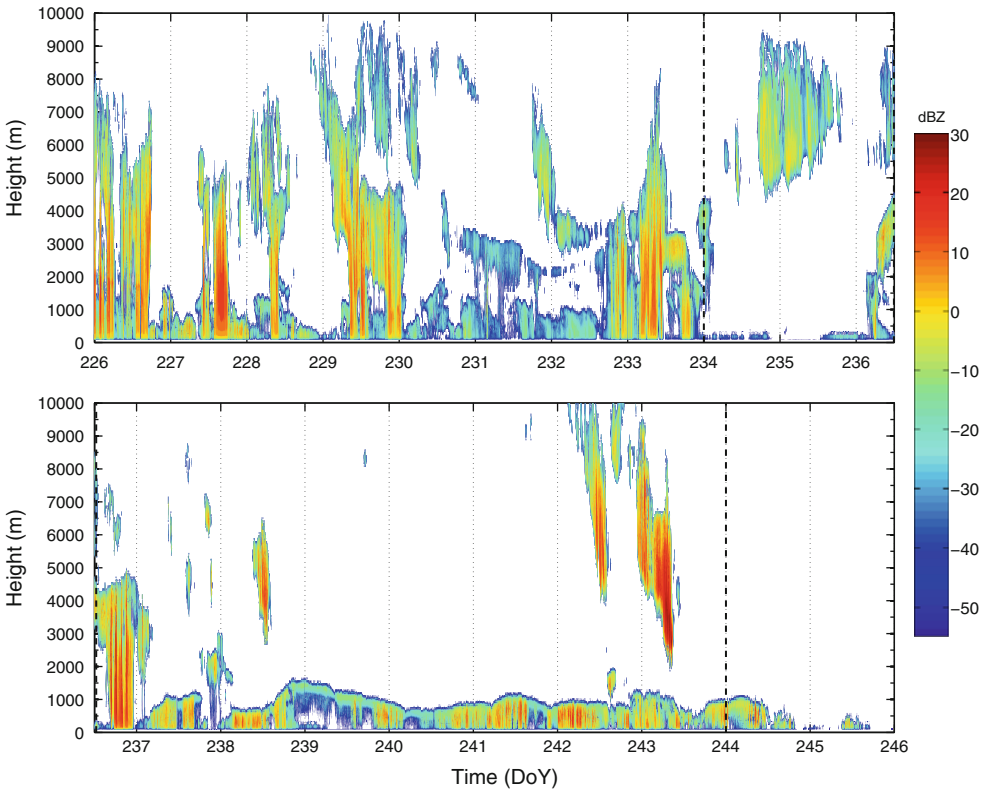


**Fig. 3** Radar reflectivity contour time series during the ice drift from the MMCR's lowest range gate at 0.105–10 km. The top panel is the first 10 days, where *dashed vertical lines* differentiate between the first two temperature regimes; the *lower panel* is a continuation in time from the *top panel*, showing the 3rd and 4th regimes. Reflectivity is sensitive to particle size to the 6th power, thus brighter contours typically represent ice crystals; these are typically larger than liquid cloud droplets

low clouds had dissipated by DoY 235, with the only identifiable clouds being the upper-level cirrus from 5,000 m up to 9,500 m at its deepest. While upper-level clouds were present around the onset (∼DoY 237) and end (∼DoY 243) of the 3rd regime, it was dominated by a lower stratiform cloud layer (Fig. 3, lower panel). At times, multiple layers were present with ice-crystals falling from a liquid layer near cloud top. The final regime from DoY 244 through 245 initially included the previous low-level stratiform cloud layer, which decreased in depth and reflectivity and became tenuous and altogether absent from the MMCR record early during DoY 245. For approximately six hours around noon on DoY 245, the low cloud layer was again visible in the cloud radar data before disappearing for the remainder of the ice drift. Like the surface temperature division, the cloud scenes observed during each respective regime bear similiarities and warrant these divisions.

Atmospheric parameters such as temperature and water vapor affect the presence and distribution of cloud cover. A comparison of mean temperature and mean water-vapor mixing ratio profiles between the relatively warm 1st and 3rd temperature regimes suggest that the temperature below 1,500 m was between 2−4°C warmer and the moisture content was higher by 0.5–1.3 g $kg^{-1}$ during the 1st regime (Fig. 4). Such shifts in the thermodynamic structure are likely associated with large-scale air-mass changes. Figure 5 shows 5-day back trajectories arriving 200 m above Oden's location for up to 2 days before and 2 days after the regime transitions. Prior to the onset of the 2nd temperature regime, the flow was from the Kara Sea (blue in Fig. 5a). Shortly after DoY 233 and near the onset of the 2nd regime, the low-level air trajectories swung around and came from northwest Greenland (red in Fig. 5a and blue in Fig. 5b). By the start of the 3rd regime, the flow arrived from the Fram Strait to the south (red in Fig. 5b). The final, cold temperature regime (DoY 244–245) coincided with an air-mass from the central Arctic basin, and beyond, with long travel times over the Arctic Ocean pack ice (red in Fig. 5c). Clearly, the three regime transitions identified in Fig. 2 are associated with transitions of the low-level air trajectories ending at Oden. Differences in the atmospheric thermodynamics, especially the reduced cloudiness during both the 2nd and 4th regimes, were coincident with these changes in synoptic-scale motions.

## 5 Energy fluxes

### 5.1 Turbulent and conductive fluxes

The mean turbulent and conductive heat fluxes were small relative to the radiative fluxes, although the variability was large (Fig. 6a–c). The magnitudes were similar to those

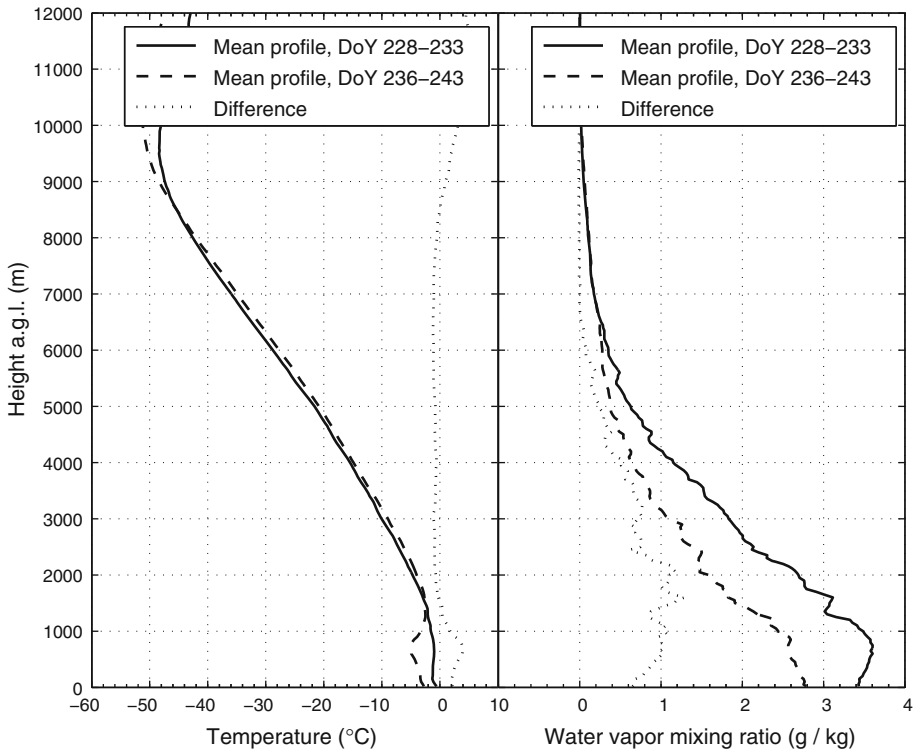


**Fig. 4** Mean temperature (°C, *left panel*) and water vapor mixing ratio (g $kg^{-1}$, *right panel*) for the 1st regime (DoY 228–233, *solid line*) and 3rd regime (DoY 236–243, *dashed line*). The *dotted line* is the difference between the mean profiles for each period

previously measured over the Arctic sea ice during this season (Intrieri et al. 2002a; Persson et al. 2002). While the latent heat flux was slightly positive on average, cooling the surface by 1 W $m^{-2}$, the mean sensible heat flux varied between −2 and 6 W $m^{-2}$. The conductive heat flux relative frequency distribution varied in a similar manner to the surface temperature, suggesting a rapid response of heat flux through the snow layer. Initially, the conductive flux was negative, directed from the surface into the ice in response to the positive surface forcing. During the cold 2nd regime, heat conduction from the ice turned positive and the snow surface gained heat previously stored within the ice. The peak in positive conductive flux coincides with the absence of low-level cloudiness. During the 3rd regime it remained slightly positive, with larger heat losses occurring again during the 4th regime. The upper ocean heat flux below the ice was most variable during the 1st and 3rd regimes, but on average only slightly larger than 1 W $m^{-2}$ from the ocean into the ice (Fig. 6d).

### 5.2 Radiative fluxes

The progression of the radiative fluxes are shown in Fig. 7. During the 1st regime, the net shortwave flux was variable and most often ranged between 10 and 40 W $m^{-2}$ (Fig. 7a), while the net longwave flux was −10 W $m^{-2}$ to near zero (Fig. 7b). The onset of the first cold regime on DoY 234 coincided with a deficit in net radiation (Fig. 7c). Net shortwave radiation temporarily increased (20–50 W $m^{-2}$) while net longwave decreased (−40 to −50 W $m^{-2}$) during DoY 235, consistent with a decrease in the cloud greenhouse effect at the time when the radar reflectivity suggested diminishing low-level clouds (Fig. 3, top panel). Mean net radiation returned to positive values during the 3rd regime, likely due to the re-emergence of low-level clouds (Fig. 3, lower panel) trapping longwave radiation near the surface. Rapid surface albedo increases were observed during the 2nd regime, due to a combination of snow-fall, freezing melt ponds and rime deposition, while SZA continually increased during the ice drift (Table 1). These factors together caused shortwave transmission through the ice to decrease following DoY 236, from approximately 3.5% of the surface downwelling irradiance before, to approximately 1.7% after (Fig. 7d). The radiative fluxes during the cold 4th regime were similar to those of the 2nd regime, coinciding again with tenuous, decreasing cloud radar reflectivity (Fig. 3, lower panel).

## 6 Cloud radiative forcing

Cloud fraction based on the backscatter intensity of the vertically pointing cloud ceilometer is shown in Fig. 8 (top panel). Nearly constant overcast skies were observed during both of the week-long 1st and 3rd regimes, demonstrating the persistent nature of Arctic cloudiness during August. The lowest cloud base was below 200 m 70% of the time and was rarely observed above 1,000 m.

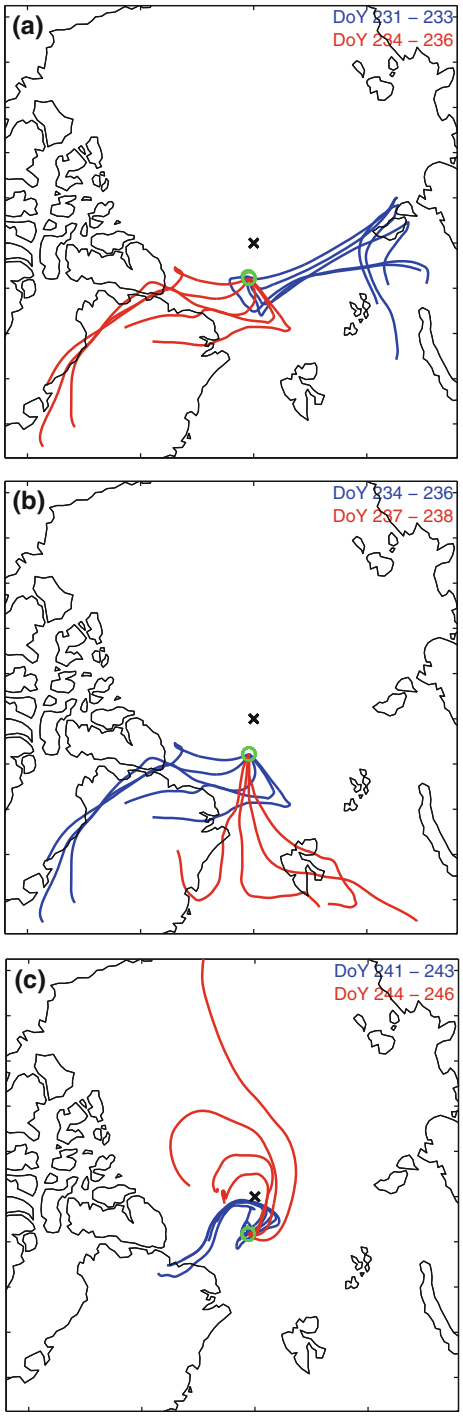


**Fig. 5** 5-day back trajectories ending at 200 m above the position of Oden, calculated for 2-day periods before (*blue*) and after (*red*) the transitions shown by the *dashed vertical lines* in Fig. 2). The *cross* and *circle* mark the north pole and Oden's position, respectively

SWF, LWF and total CRF are shown in the lower panel of Fig. 8. Each of the four regimes are characterized by distinct CRF patterns; the 1st and 3rd regimes exhibit comparable forcing behavior. SWF, ranging from −50 to −25 W m$^{-2}$, was largest during the 1st regime, after which increased surface albedo and SZA (Table 1) by the start of the 3rd regime caused a decrease in SWF by more than a factor of two relative to the 1st regime. A diurnal cycle in SWF indicates a significant dependence on SZA, with the diurnal amplitude of about 15–22 W m$^{-2}$ at the beginning decreasing to about 10–12 W m$^{-2}$ at the end of the ice drift, similar to values reported by Shupe and Intrieri 2004.

LWF generally ranged between 65 and 80 W m$^{-2}$ during the 1st regime, and between 70 and 85 W m$^{-2}$ during the 3rd regime. Mean LWF during the 3rd regime was ∼76 W m$^{-2}$, nearly 5 W m$^{-2}$ larger and statistically significant than during the 1st regime. As discussed above, considerable differences in the lower atmospheric thermal structure were observed during these two regimes. As a result of warmer temperatures and higher water vapor content in the lowest few kilometers, longwave clear-sky atmospheric radiative emission is enhanced during the 1st regime compare to the 3rd, partially masking the cloud LWF during the 1st regime. This is consistent with the findings of Zhang et al. (2001). Total CRF reflected this shift in both SWF and LWF. Clouds warmed the surface by 25–55 W m$^{-2}$ during the 1st regime; this increased to 55–75 W m$^{-2}$ during the 3rd regime (Fig. 8, black line).

The magnitudes of SWF and LWF decreased temporarily on DoY's 234 and 235. A SWF of 25 W m$^{-2}$ at the start of this regime decreased to −10 to −5 W m$^{-2}$ as low-level clouds thinned or disappeared (Fig. 3). LWF simultaneously dropped from ∼75 W m$^{-2}$ to nearly 10 W m$^{-2}$, and together the total CRF decreased from ∼50 W m$^{-2}$ to near zero. Similarly, both cloud radiative forcing components decreased during the cold 4th regime. Here, LWF decreased from ∼80 to 10 W m$^{-2}$ and SWF from −20 W m$^{-2}$ to near zero. Since the mean SWF varied by, at most, 25 W m$^{-2}$ during both cold regimes, LWF was responsible for the majority of the change in total CRF, underlining the importance of the cloud LWF at this time of year. Even with uncertainty estimates on the order of 10–15 W m$^{-2}$ as described in 3, CRF estimates indicate a robust cloud-warming effect at the surface during ASCOS.

## 6.1 Cloud forcing sensitivity

### *6.1.1 SWF sensitivity*

It is important to understand how the critical factors influencing SWF and LWF affect the total CRF at the surface. SWF depends on the cloud microphysical properties, the surface albedo and the SZA (Curry et al. 1996). Figure 9 shows the influence of SZA, surface albedo and LWP on SWF. The range of SWF agrees well with the average range reported during SHEBA for similar SZAs (Shupe and Intrieri 2004). The magnitude of shortwave forcing generally increases with decreasing surface albedo,

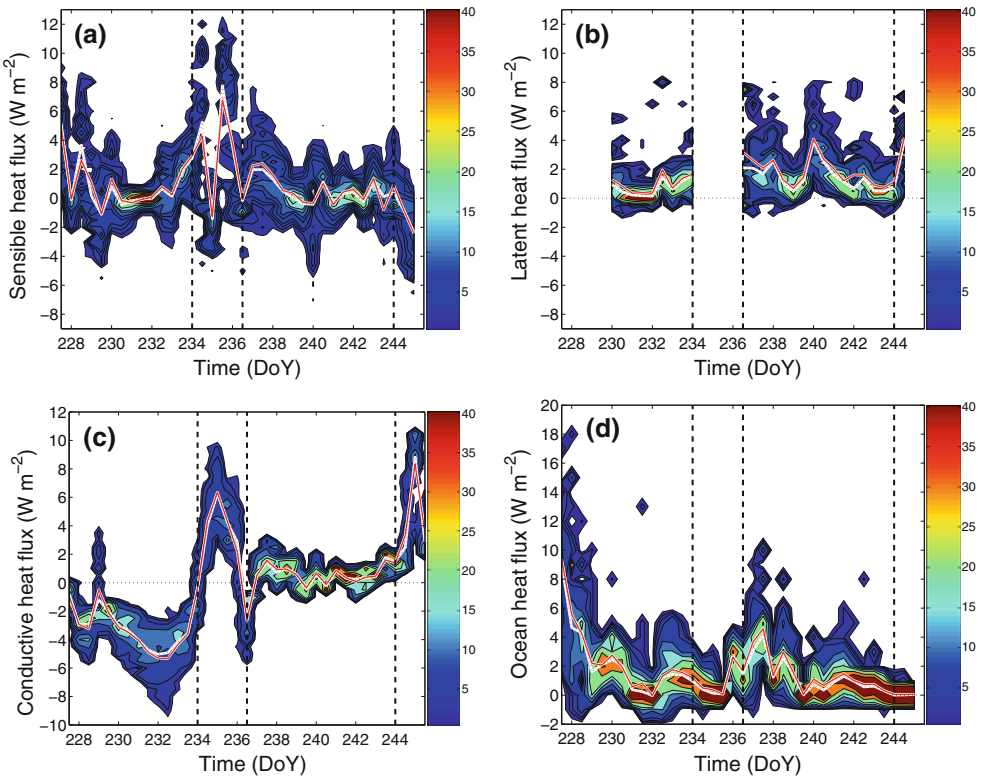


**Fig. 6** Relative frequency distribution time trace for **a** sensible, **b** latent, **c** conductive and **d** oceanic heat flux, all given in W m$^{-2}$. *Colors* represent probability of occurrence for a given heat flux as function of DoY, calculated over 12-h non-overlapping intervals. *Solid* and *dotted red lines* represent the 12-h mean and median fluxes, respectively. *Dashed vertical lines* indicate the division of regimes

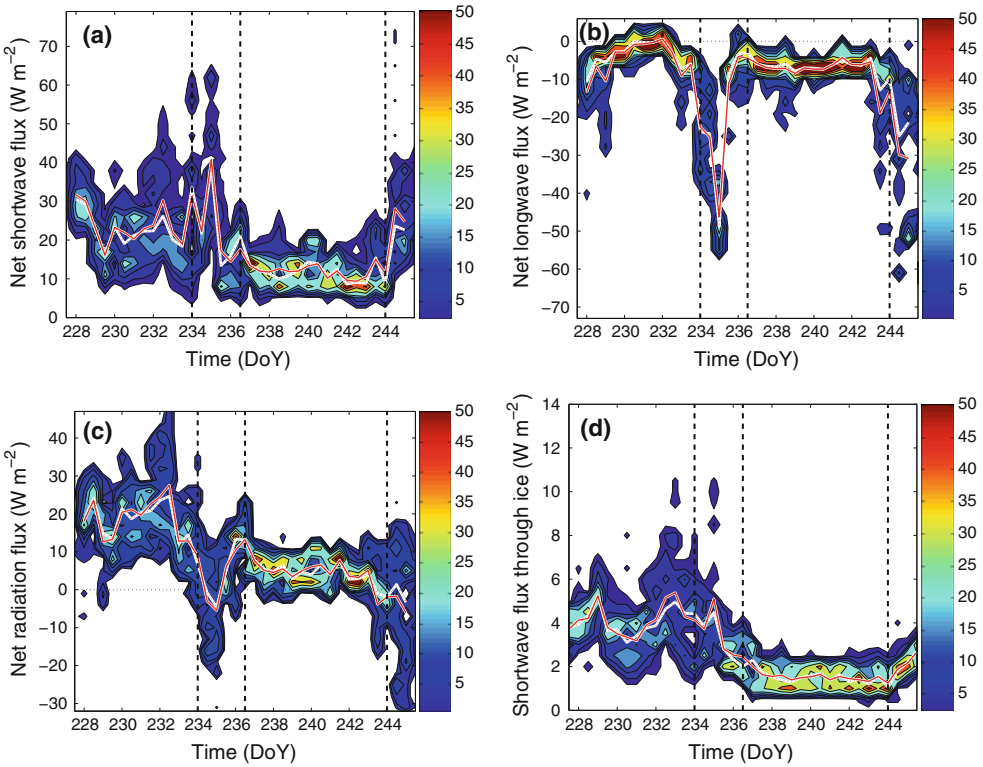


**Fig. 7** Same as in Fig. 6 except for **a** net shortwave, **b** net longwave, **c** total net and **d** shortwave radiation transmission through the ice

such that a linear fit of the forcing to surface albedo results in an increased SWF of $\sim$1.8 W m$^{-2}$ for every 0.01 decrease in surface albedo. However, as the data suggests, the change in forcing for a particular surface albedo also depends, to a large extent, on the SZA. During times of relatively lower surface albedo, the variation in SWF with SZA ranged from 15 to 20 W m$^{-2}$, while this forcing sensitivity decreased to near 10 W m$^{-2}$ for larger albedo.

**Table 1** Regime classification (DoY-Day of Year), corresponding statistics of surface albedo $\alpha_s$ (including standard deviation $\sigma$ and percentiles), solar zenith angle (SZA) range and the energy budget flux components for both snow and the ice, all in W m$^{-2}$

| Time (DoY) | Mean $\alpha_s$ ($\sigma$) | Median $\alpha_s$ (25th, 75th) | SZA (°) | Energy budget fluxes for the snow/ice (W m$^{-2}$) | | | | | |
|---|---|---|---|---|---|---|---|---|---|
| | | | | $R_s$ | $R_l$ | $H_s$ | $H_l$ | $H_c/H_o$ | Residual |
| 227–233 | 0.75 (0.03) | 0.74 (0.73, 0.77) | 73.8–80.1 | 23.9/20.2 | −4.4 | −1.0 | −0.6 | −3.6/2.4 | 14.3/16.6 |
| 234–236.5 | 0.81 (0.02) | 0.82 (0.80, 0.82) | 75.4–81.2 | 29.3/26.8 | −25.8 | −3.7 | −1.2 | 3.7/0.7 | 2.9/−3.4 |
| 236.5–243 | 0.85 (0.02) | 0.85 (0.84, 0.86) | 76.4–83.8 | 11.7/10.4 | −7.5 | −0.6 | −1.4 | 0.6/1.5 | 2.8/2.4 |
| 244–245 | 0.84 (0.02) | 0.84 (0.83, 0.85) | 78.6–85.0 | 25.0/23.6 | −30.2 | 0.9 | −0.5 | 3.9/0.1 | −0.9/−6.2 |

Energy budget components are defined as in Eqs. 1–2

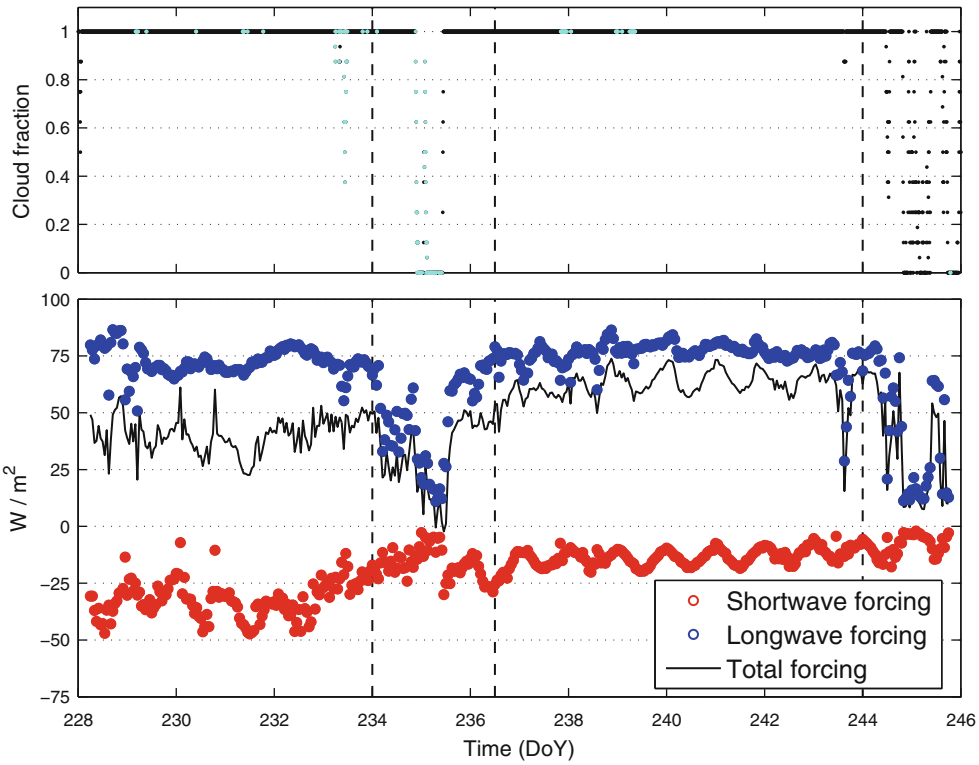


**Fig. 8** *Top panel* 10-min cloud fraction (0–1) with cloud bases <1,000 m (*black dots*) and cloud bases >1,000 m (*turquoise dots*). *Lower panel* SWF (*red circles*), LWF (*blue circles*) and total CRF (*black line*), all in W m$^{-2}$

SWF estimates are also dependent on the cloud properities which act to reflect, absorp and transmit shortwave radiation. In a general sense, clouds with larger LWP yield a larger SWF and more strongly cooled the surface, although the variability in Fig. 9 shows how SWF is a combination of all controlling factors. The net surface shortwave flux in the absence of an atmosphere is proportional to the solar constant times the product of the cosine of SZA and the surface albedo (Shupe and Intrieri 2004). Therefore, to examine the combined effect of SZA and surface albedo influences on SWF, we plot SWF versus the non-dimensional product of cos(SZA) and (1-albedo) (Fig. 10a). The majority of data points are nearly linearly proportional to this scaling parameter; only some cases with low LWP exhibit smaller SWF. This result is further supported by a plot of the downwelling shortwave cloud attenuation, defined as the observed minus clear-sky downwelling shortwave normalized by the top of the atmosphere shortwave radiation which also shows a significant dependence on cloud LWP (Fig. 10b). After having excluded the external parameters of surface albedo and SZA, the remaining variability in the shortwave cloud attentuation results from variations in cloud geometry, droplet size and phase. Thus cloud structure and composition itself, not only the large SZAs and surface albedo, are also responsible for complex cloud-radiative interactions over the Arctic.

### 6.1.2 *LWF sensitivity*

LWF is largely influenced by the cloud's emissivity dependence on LWP, cloud droplet radius and phase, along

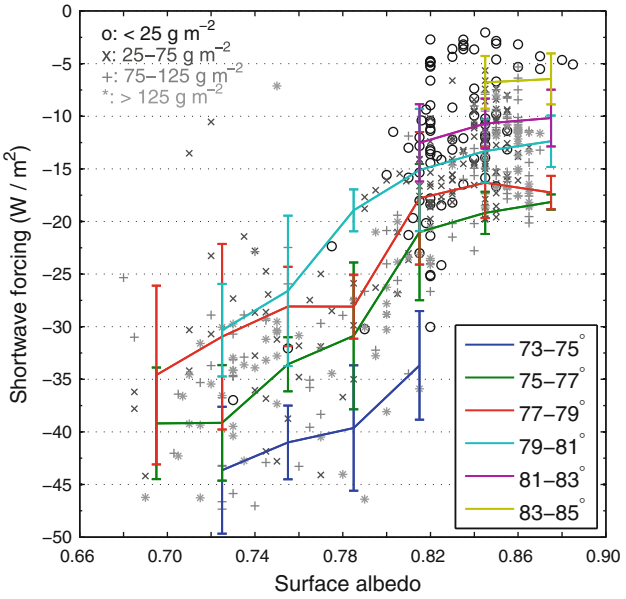


**Fig. 9** One hour SWF as a function of surface albedo. SWF data have *symbols* and *shading* for different ranges of cloud LWP (g m$^{-2}$), shown in the *top left corner*. *Colored lines* represent bin-averaged SWF for solar zenith angle (SZA) ranges shown in the *lower right legend*, and *error bars* represent ±1 SD of the SWF for each 0.03 bin of surface albedo. All forcing in W m$^{-2}$

with the emission temperature of the cloud. As discussed above, the clear-sky downwelling longwave radiation can further act to modulate the LWF. Figure 11 shows the dependency of LWF on LWP, separated into cloud-base temperature ranges, determined by interpolated radiosonde profiles and ceilometer-determined cloud-base heights. In general, LWF estimates were on the order of 10 W m$^{-2}$ larger during ASCOS than those computed at SHEBA for the similar season and for LWP above 50 g m$^{-2}$ (Shupe and Intrieri 2004; Chen et al. 2006). LWF increases significantly when LWP increases from near zero to ~50 g m$^{-2}$, corresponding to an exponential dependence of cloud longwave emissivity on LWP for liquid-containing clouds (e.g. Stephens 1978). Further increases in LWP exert no significant impact on LWF as the cloud radiates as a nearly-ideal black body (Garrett et al. 2002; Shupe and Intrieri 2004). LWF from clouds with base temperatures below −10°C was small since these clouds typically contained only a limited amount of liquid. The range in LWF for LWP >50 g m$^{-2}$ was largest for cloud-base temperatures ranging from −5 to 0°C. The lower data points for LWF within the cloud-base temperature range of −5 to 0°C occurred primarily during the 1st regime when a warmer and moister atmosphere partly masked enhanced downwelling longwave flux from the cloud. On the other hand, the higher LWF for this temperature range came about during the 3rd regime, characterized by fog or low-level cloud layers with slightly warmer cloud-base temperatures. These low layers were the cause of LWF in excess of 75 W m$^{-2}$ even when LWP was <50 g m$^{-2}$.

## 7 Snow and ice energy budgets

Means for the terms in Eqs. 1 and 2 across the four regimes are shown both for the snow surface (Fig. 12a) and the sea ice (Fig. 12b), including ±1 standard deviation bars. Generally speaking, the two mean energy budgets show similar trends (see Table 1). The dominance of the radiative fluxes over the turbulent and conductive fluxes is especially apparent during the cold 2nd and 4th regimes,

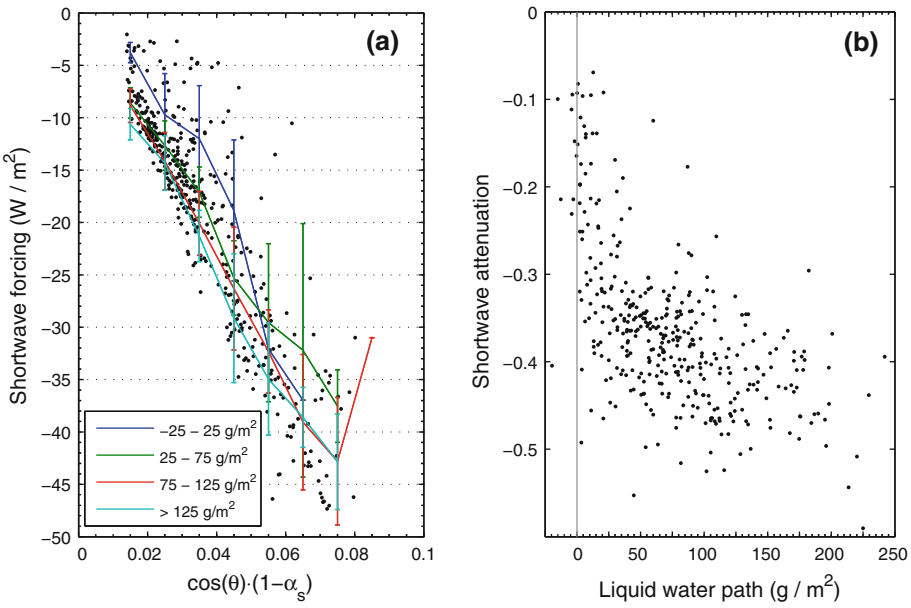


**Fig. 10** **a** One hour SWF (W m$^{-2}$) dependence on the linear relationship between SZA ($\theta$) and surface albedo ($\alpha_s$) and **b** non-dimensional shortwave attenuation as a function of cloud LWP (g m$^{-2}$). Shortwave attenuation is the difference between observed and clear-sky downwelling shortwave radiation normalized by the top of atmosphere downwelling shortwave radiation, providing a measure of cloud reflectivity of shortwave radiation

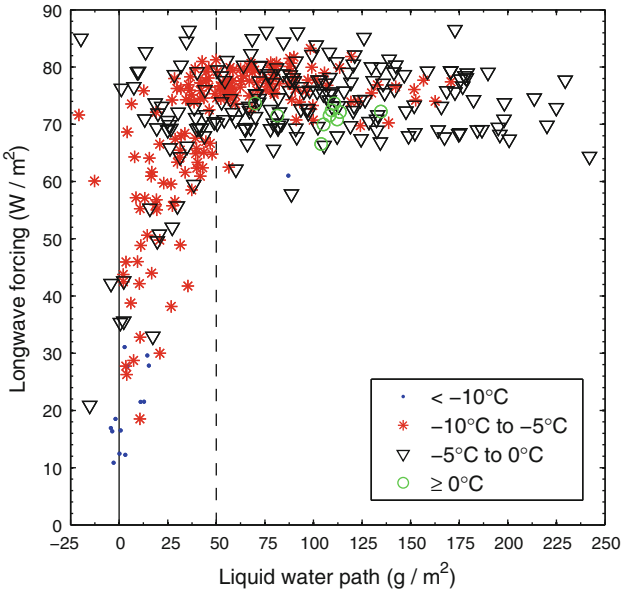


**Fig. 11** One-hour LWF (W m$^{-2}$) as a function of cloud LWP (g m$^{-2}$), separated by cloud base temperature ranges from <−10 to >0°C. The *solid vertical line* represents the zero LWP line; LWP <0 g m$^{-2}$ are included due to the 25 W m$^{-2}$ uncertainty in the measurement. The *dashed vertical line* marks a LWP of 50 g m$^{-2}$ (see *text*)

although the variability was also greatest and larger than the mean radiative fluxes. According to the net residual energy fluxes, both the snow and the ice underwent a substantial transition during the ice drift. A mean surplus of 14 W m$^{-2}$ was available for surface snow melt during the 1st regime (Fig. 12a). Lower SZA and surface albedo permitted the surface to absorb and transmit a significant fraction of the transmitted shortwave radiation.

A residual of 14 W m$^{-2}$ at the surface corresponds to approximately 4 cm of snow melt per day if we assume a frozen-to-liquid snow density ratio of 10:1 (cf. Roebber et al. 2003). Note that this is likely an overestimate because we ignore shortwave radiation penetrating through the snow and ice. Significant frontal precipitation and falling ice crystals from low-level mixed-phase clouds prior to DoY 232 could have offset this snow melt. The total residual for the ice and snow system as a whole was 17 W m$^{-2}$, indicating that the majority of the heat was expended in melting the upper snow layer.

The three subsequent regimes experienced significantly smaller net snow and ice residuals (Fig. 12 and Table 1). Increased losses of heat associated with decreasing cloud cover yielded mean net radiative fluxes that nearly offset

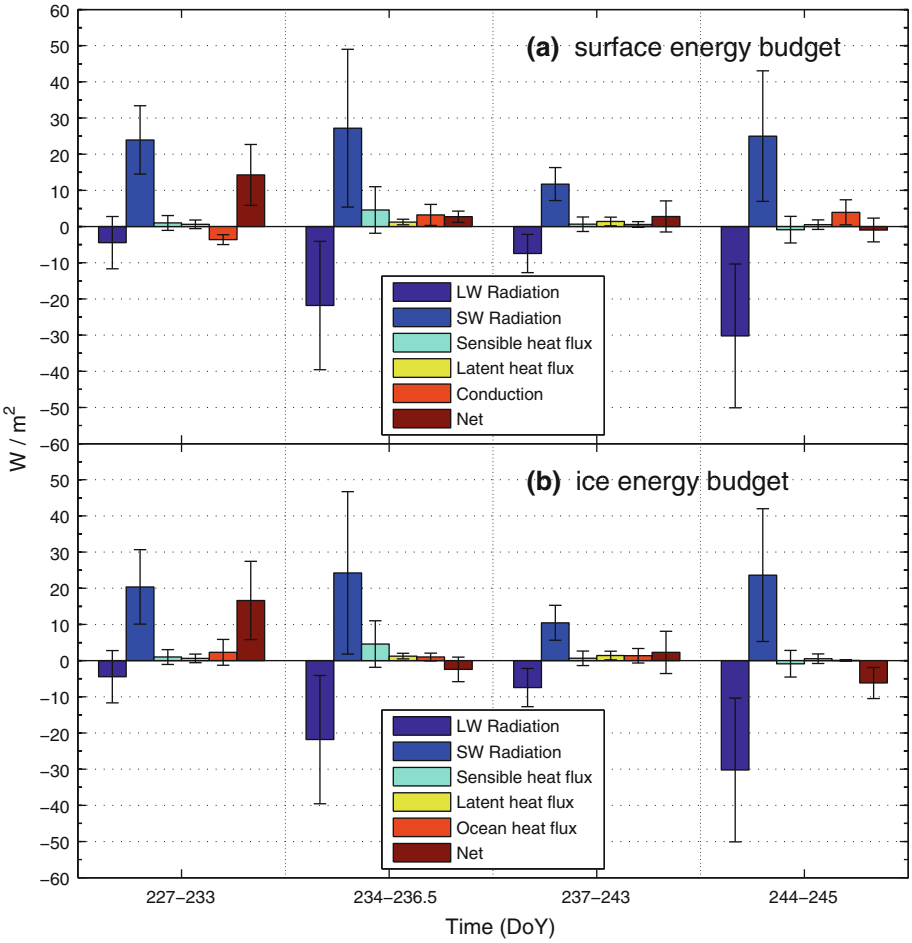


**Fig. 12** Mean components of the energy budget terms for **a** the snow surface and for the **b** sea ice in W m$^{-2}$ calculated over the four main regimes identified in Sect. 4. Positive flux represents a warming and negative flux a cooling, except for sensible and latent heat fluxes, which are defined traditionally where positive is cooling. The snow surface budget includes conduction but excludes ocean heat flux and transmission of shortwave radiation. The ice budget includes ocean heat flux and transmission of solar radiation but excludes conduction. Black variability bars represent ±1 standard deviation of the mean fluxes for each respective regime

each other during the cold regimes. As a result, heat previously stored within the ice was transferred upwards to compensate surface energy loss, resulting in a negative residual for the ice. Thus, the first potential indication of freeze-onset occurred between DoY 234 and 235. However, the surface residual remained slightly positive during the 2nd regime, but we know this surface estimate to be biased warm. The mean residuals during the 3rd regime were small; the variability is larger than the mean value which is not significantly different from zero. An increase in the mean surface albedo from 0.73 to 0.84 occurred during and after the 2nd regime through a combination of freezing melt ponds, rime deposition and new snow fall. By the 4th regime, both mean heat budget residuals were negative due to large deficits in net longwave radiation and a reduction in net shortwave radiation. Turbulent heat fluxes were nearly the same magnitude as both the net radiative and residual fluxes for all but the first regime, implying that the turbulent fluxes act as significant redistributors of the total radiative forcing. Despite variability in the observations, both snow and ice residuals were negative and corresponding temperatures decreased significantly, suggesting that full initiation of the fall freeze-up occurred during the 4th regime, approximately 10 days after the first indication of freeze. We shall return to this temporal difference in the discussion below.

## 8 Case study

We have demonstrated that the surface energy budget system is largely influenced by the presence, absence and properties of the cloud cover. To illustrate this influence, we investigate DoY 235. A cirrus cloud, sometimes more than 4,000 m thick, was overhead during much of this 24-h period (Fig. 13a). Tenuous low-level clouds were observed by the ceilometer and MMCR in the early morning hours and again after 12 UTC, as an increasingly robust fog deepened into a low-level cloud below 300 m. There was little or no cloud liquid water (Fig. 13e) identifiable until after 12 UTC, coincident with the developing low-level cloud. Analysis of upper-level radiosoundings suggests that colder air was advected over the ice drift during the morning and early afternoon hours, which may have provided the necessary cooling for saturation of liquid water.

Surface temperature varied approximately between −7.5 and −6°C (Fig. 13b) prior to 12 UTC, and a linear fit to these first 12 h suggests no temporal trend. Shortly before 12 UTC surface temperature jumped and continued on an increasing trend through the remainder of the 24-h period, although the absolute change in temperature during the afternoon was only slightly larger than 2°C. The downwelling radiative fluxes (Fig. 13c, d) are significantly modified by the cloud scene overhead, and surface responds to these radiative changes. Temperatures below −6°C were generally associated with a negative net radiative flux ranging from −35 to 0 W $m^{-2}$ (Fig. 14a), and LWP was typically no larger than 15 g $m^{-2}$ (Fig. 14b). The lack of robust liquid clouds permitted a larger net shortwave flux, while the reduction in cloud greenhouse warming resulted in net longwave deficits of more than −50 W $m^{-2}$. The lack of a liquid-rich cloud scene resulted in CRF near zero (Fig. 14a) and estimates of the total surface energy residual before 12 UTC were generally larger than −20 W $m^{-2}$ (median value −13 W $m^{-2}$), suggesting that surface radiative forcing resulted in a redistribution of turbulent and conductive heat fluxes which effectively limited the absolute change in surface temperature (Fig. 14c). Temperatures above −6°C generally occurred as cloud LWP increased with the deepening lower cloud layer, yielding small but positive net radiation at the surface as a result of a net cloud radiative forcing change of ∼30 W $m^{-2}$. The corresponding change in total surface energy was approximately half of this net radiative forcing change, however the surface temperature increase was limited to only ∼2°C. In-ice temperatures, as well as estimates using an equivalent snow depth, suggest that a thermal wave in response to the surface forcing penetrated through the snow and into the ice, but only within the uppermost 10 cm below the surface. Given the change in residual forcing of 15 W $m^{-2}$ and assuming reasonable snow depth, the estimated surface temperature increase should not have been larger than 3°C, in line with the observed temperature increase. Although this case is not representative of the entire ASCOS ice drift, it demonstrates how periods of tenuous, or absent, clouds with little liquid water can "force" the coldest temperature regimes and effectively initiate the system into, or out of, a freeze-up transition for the conditions encountered.

Sensible heat (Fig. 13f) was transferred from the atmosphere towards the surface prior to 09 UTC and then changed sign and remained positive after 10:30 UTC. This is coincident with an increase in cloud LWP from 0 to 10 g $m^{-2}$ (Fig. 13e), which caused downwelling longwave radiation to increase by ∼20 W $m^{-2}$ (Fig. 13d). The surface energy balance, forced mainly by the reduction in net longwave deficit due to the developing low cloud, led to a warming of the surface, more quickly than the near-surface air. This caused a destabilization and transitioning from stably stratified to convective conditions. Radiosonde profiles during the day suggest that the modification of the energy at the surface led to a deepening ABL from less than 100 m in the morning to approximately 200 m in the afternoon (Fig. 15, top panel). The sodar backscatter (Fig. 15, lower panel) confirms the shallow boundary-layer depths in the morning; strong acoustic backscatter is an

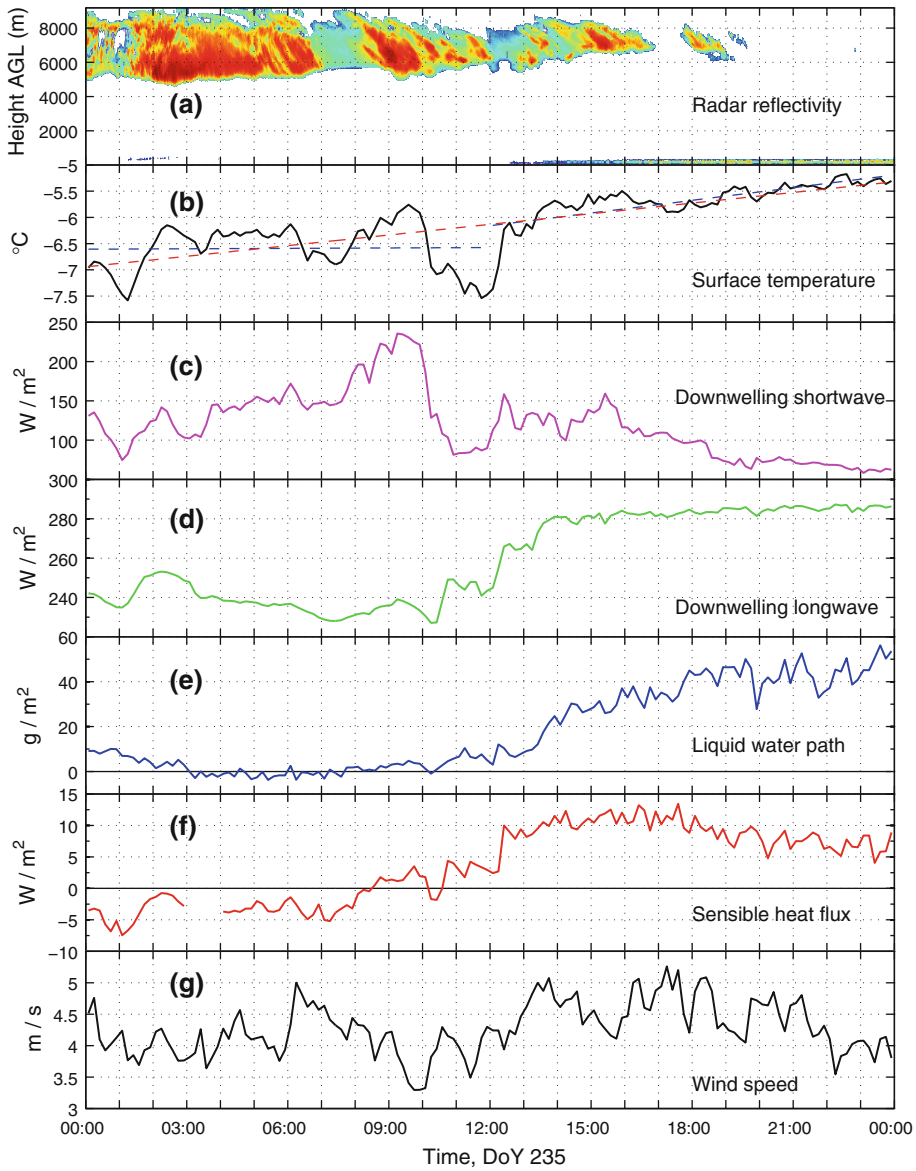


**Fig. 13** Time traces of **a** MMCR reflectivity (*dBZ contours*), **b** surface temperature (°C *black*) and linear-fit temperature trends for 12-h (*dashed blue*) and 24-h intervals (*dashed red*), downwelling **c** shortwave and **d** longwave radiation (W $m^{-2}$), **e** MWR retrieved liquid water path (g $m^{-2}$), **f** sensible heat flux (W $m^{-2}$) and **g** 30 m wind speed (m $s^{-1}$) during DoY 235. Note that the cloud radar reflectivity scale is not the same as in Fig. 3; the *reddest reflectivity contour* here corresponds to −1 dBZ

indication of temperature variance associated with turbulence acting in a strong gradient and is commonly observed at the interface between the boundary layer and free troposphere. The increased ABL depth to over 200 m in the afternoon, seen in both temperature and sodar backscatter profiles, coincides with the vertical location of the deepening low-level cloud layer during the afternoon. Considering the negligible changes in the near-surface wind speed over the course of the day (Fig. 13g), these results suggest that neither advection of heat nor increased mechanical mixing directly forced the surface temperature increase on this day. Instead, surface cloud radiative forcing destabilized the lower boundary layer and caused a vertical turbulent transport of sensible heat. However, it can be argued that cold-air advection aloft may have been responsible for the low-level cloud development.

## 9 Discussion and conclusions

The duration of the Arctic melt season and the timing of the autumn freeze-up onset have significant impacts on the Arctic surface heat budget. The transitioning energy budget components of both the snow surface and the sea ice have been analyzed using measurements from the ASCOS campaign. Surface cloud radiative forcing was calculated with the use of a radiative transfer model. The influence of the solar and surface conditions and the cloud liquid water path on the cloud short- and long-wave radiative forcing components was determined.

Clear transitions between different regimes are evident in the surface temperature. The radiative fluxes support a division into four distinct regimes characterized by differing thermodynamic structure and cloud properties. These

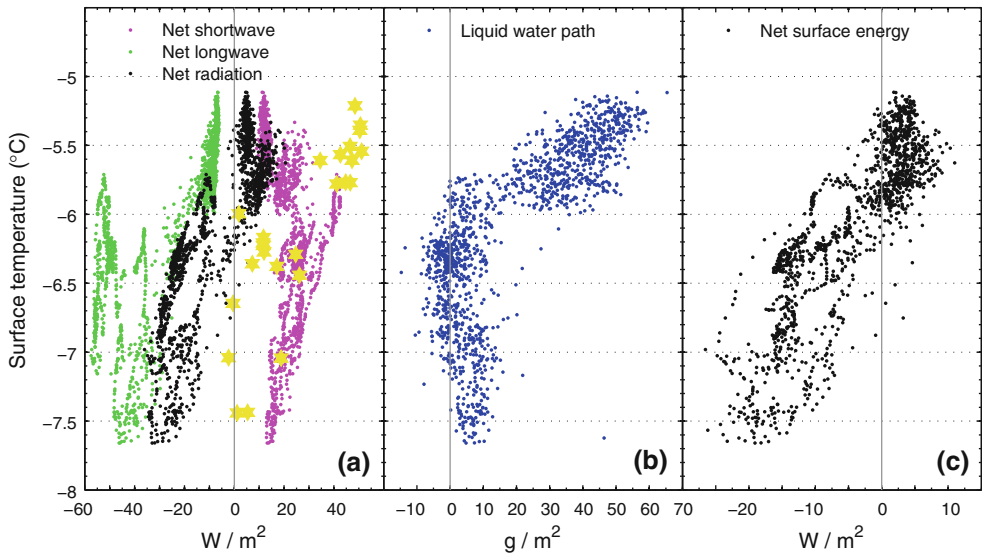


**Fig. 14** One minute averaged surface temperature (°C) as a function of **a** net radiative fluxes (W $m^{-2}$), **b** LWP (g $m^{-2}$) and **c** total surface energy residual (W $m^{-2}$) during DoY 235. *Yellow hexagrams* in **a**) represent the 1-h CRF estimates and associated surface temperature

regimes are linked to changes in synoptic-scale weather patterns modifying the temperature and humidity profiles and the accompanying cloud field. We have identified a large-scale shift in the atmospheric thermodynamic structure between the 1st and 3rd weeks of the ice drift. Back trajectory calculations indicate the flow was from the Greenland and Barent Seas during the 1st week, bringing warmer and more humid air masses associated with a series of synoptic fronts. This flow pattern continued early in week 3, but became increasingly more influenced by a high pressure advecting over the central Arctic from Greenland, associated with a cooler and drier lower troposphere. In response to the varying cloudiness, the radiative fluxes showed the largest variations and dominated the energy budgets. Net shortwave radiation generally ranged between 10 and 40 W $m^{-2}$ when cloud cover was present, but could be significantly larger when cloud cover was tenuous or absent, as observed during the two cold regimes. The magnitudes of shortwave effects decreased with time as SZA and surface albedo increased. Net longwave radiation when clouds were present consistently ranged from −10 to 0 W $m^{-2}$, but the deficit was observed to reach as much as −60 W $m^{-2}$ during tenuous cloud periods. The turbulent and conductive fluxes were significantly smaller than these, although they were on the same order as the mean net energy fluxes for three of the four regimes, making them significant redistributors of the energy imparted by radiative fluxes.

Total CRF ranged from approximately 25–50 W $m^{-2}$ during the 1st regime, and the magnitude increased to 55–75 W $m^{-2}$ during the 3rd regime. The increase in forcing magnitude was related to variations in both SWF and LWF components. Mean surface albedo increased from ∼0.73 to ∼0.84, limiting the shortwave radiation absorption at the surface, and at the same time the SZA continued to increase, reducing the amount of incident shortwave radiation. The influences of SZA and the surface albedo on SWF, along with the influence of cloud LWP have been examined. The forcing generally increased linearly in combination with increasing LWP and decreasing SZA and surface albedo. SWF exhibited a diurnal cycle of 10–22 W $m^{-2}$, being largest when SZA and surface albedo were smallest. Mean LWF increased by approximately 5 W $m^{-2}$ during the ice drift and has been linked to a decrease in the background atmospheric temperature and humidity, which masked a part of the LWF during the 1st regime. However, downwelling longwave radiation did decrease during the 3rd regime relative to the 1st and can be attributed to advection of cooler air in the lower troposphere.

The surface temperature changes during the deployment were found to be largely controlled by (1) the enhancement of downwelling longwave radiative flux emitted from low clouds, (2) the changing reflectivity of the ice surface and (3) the sun angle. When clouds were tenuous or temporarily absent, deficits in net longwave radiation at the surface overwhelmed increases in solar heating, causing the surface temperature to drop rapidly. On the contrary, enhanced emission of downwelling longwave radiation from low clouds with increasing cloud liquid water yielded small, but slightly positive net radiation. A combination of positive net radiation and conduction of heat from within the sea-ice to the snow-surface results in a relative surface warming, a dynamical response observed during the cold-

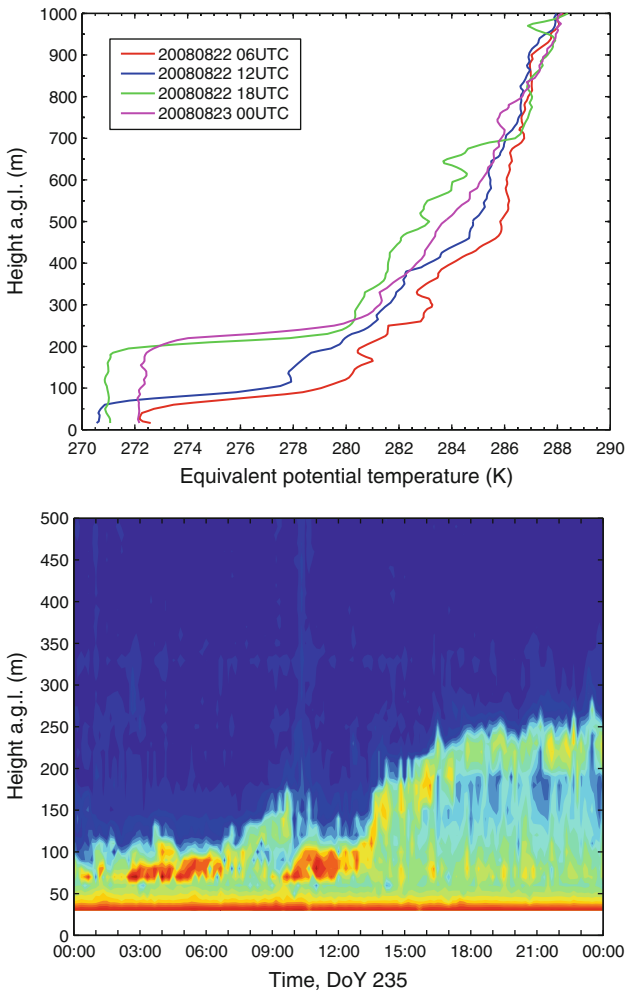


**Fig. 15** Equivalent potential temperature profiles (K, *top panel*) during 22 August 2008 (DoY 235) from 6-h radiosonde releases: 06 UTC (*red line*), 12 UTC (*blue line*), 18 UTC (*green line*) and 00 UTC 23 August 2008 (*magenta line*). *Lower panel* time trace of acoustic backscatter from the sodar (dB, arbitrary units; higher power is *brighter colors*)

temperature regimes although the warming magnitude can be limited by changes in turbulent fluxes. When the surface warmed quicker than the air, a destabilization of the lower atmosphere occurred and turbulent heat fluxes increased in magnitude, cooling the surface.

Mean energy budget residuals suggest that the initial freeze onset could have begun during the cold 2nd regime, from 21–23 August. Climatological studies using both active and passive satellite measurements and surface temperature observations show a general consensus that interior, central Arctic freeze onset often occurs between the 2nd week of August and early September (Rigor et al. 2000; Belchansky et al. 2004; Overland et al. 2008). Observational studies often use the first instance when a running mean near-surface temperature surpasses the −2°C threshold to identify the freeze-up onset. Doing the same for the ASCOS ice drift suggests the freeze onset occurred early on 24 August (DoY 237). This date is similar to that determined with respect to the mean energy budget residual analysis of the sea ice and consistent with previous central Arctic freeze dates reported in the literature (Rigor et al. 2000; Nilsson et al. 2001; Belchansky et al 2004; Overland et al. 2008; Markus et al. 2009). The successive progression of the freeze-up during ASCOS was inhibited by low-level stratiform cloud cover during the 3rd regime, causing small but positive energy residuals.

The seasonal freeze-up onset, when temperatures no longer return to the melting point of sea-ice, appears to have happened a week or more after the cold 2nd regime, coinciding with the arrival of drier air with a long residence time in the central Arctic and optically thinner clouds or clear skies. During this 4th temperature regime, both the mean snow and ice energy budget residuals were negative. Markus et al. (2009) have demonstrated that the first indication of freeze, on average, occurs approximately 10 days prior to the time when freeze is observed to persist for the remainder of the season. The 10-day time scale observed may be related to the passage of large-scale weather systems responsible for thermodynamic advection that affects the cloud properties. We have highlighted the processes responsible for this first freeze onset and the transition toward persistent freeze during ASCOS.

The two cold-temperature regimes were associated with tenuous cloud cover, leading to reduced net warming by the clouds and subsequent drops in surface temperature. Direct deposition, or riming, of water vapor on the snow surface and ice growth on melt ponds and open leads increased the surface albedo at these times, resulting in a lower net surface shortwave radiation. Heat transfer upwards through the ice and turbulent heat fluxes from the atmosphere to the surface during the final cold regime were insufficient to compensate for the radiative cooling of the surface. Therefore, the clouds, or lack thereof, played a central role for the surface energy budget and the onset of the freeze-up, and we find cloud cover to be a key component in the surface energy budget transitions of the Arctic.

**Acknowledgments** This work is part of ASCOS (the Arctic Summer Cloud Ocean Study) and was funded by the Swedish Science Research Council and the DAMOCLES European Union 6th Framework Program Integrated Research Project. ASCOS was made possible by funding from the Knut and Alice Wallenberg Foundation. IMB and CEB were also funded by the UK Natural Environment Research Council; CEB was additionally partially supported by the UK Met Office that also provided real-time weather forecasting for ASCOS. POGP and MDS were also funded by the National Science Foundation. MN also received funding through the NorClim project, financed in the Norklima program of the Norwegian Research Council; Sebastian Gerland is acknowledged for dual-responsibility of data with MN. The Swedish Polar Research Secretariat (SPRS)

provided access to the icebreaker Oden and logistical support. Chief Scientists were Caroline Leck and Michael Tjernström. We are grateful to the SPRS logistical staff and to Oden's Captain Mattias Peterson and his crew. ASCOS is an IPY project under the AICIA-IPY umbrella and an endorsed SOLAS project.

## References

ACIA (2005) Arctic climate impact assesment: impacts of a warming Arctic. Cambridge University Press, Cambridge

Andreas EL, Jordan RE, Makshtas AP (2005) Parameterizing turbulent exchange over sea ice: the ice station weddell results. Boundary Layer Meteorol 114:439–460

Belchansky GI, Douglas DC, Platonov NG (2004) Duration of the Arctic sea ice melt season: regional and interannual variability, 1979–2001. J Clim 17:67–80

Birch CE, Brooks IM, Tjernström M, Milton SF, Earnshaw P, Söderberg S, Persson POG (2009) The performance of a global and mesoscale model over the central Arctic Ocean during late summer. J Geophys Res 114:12104. doi:10.1029/2008JD010790

Chen Y, Aires F, Francis JA, Miller JR (2006) Observed relationships between Arctic longwave cloud forcing and cloud parameters using a neural network. J Clim 19:4087–4104

Curry JA, Rossow WB, Randall D, Schramm JL (1996) Overview of Arctic cloud and radiation characteristics. J Clim 9:1731–1764

Fu Q, Liou KN (1992) The correlated k-distribution method for radiative transfer in nonhomogeneous atmospheres. J Atmos Sci 49:2139–2156

Garrett TJ, Radke LF, Hobbs PV (2002) Aerosol effects on cloud emissivity and surface longwave heating in the Arctic. J Atmos Sci 59:769–778

Graversen RG (2006) Do changes in the midlatitude circulation have any impact on the Arctic surface air temperature trend? J Clim 19:5422–5438

Graversen RG, Wang M (2009) Polar amplification in a coupled climate model with locked albedo. Clim Dyn 33:629–643

Graversen RG, Mauritsen T, Tjernström M, Källen E, Svensson G (2008) Vertical structure of recent Arctic warming. Nature 451:53–57

Intrieri JM, Fairall CW, Shupe MD, Persson POG, Andreas EL, Guest PS, Moritz RE (2002a) An annual cycle of Arctic surface cloud forcing at SHEBA. J Geophys Res 107:C10. doi:10.1029/2000JC000439

Intrieri JM, Shupe MD, Uttal T, McCarty BJ (2002b) An annual cycle of Arctic cloud characteristics observed by radar and lidar at SHEBA. J Geophys Res 107:C10. doi:10.1029/2000JC000423

IPCC (2007) Intergovernmental panel on climate change, fourth assessment report—the physical science basis. Cambridge University Press, Cambridge

Kay J, L'Ecuyer ET, Gettelman A, Stephens G, O'Dell C (2008) The contribution of cloud and radiation anomalies to the 2007 Arctic sea ice extent minimum. Geophys Res Let 35:L08503. doi:10.1029/2008GL033451

Kay JE, Gettelman A (2009) Cloud influence on and response to seasonal Arctic sea ice loss. J Geophys Res 114:D18204. doi:10.1029/2009JD011773

Leck C, Bigg EK, Covert DS, Heintzenberg J, Maenhaut W, Nilsson ED, Wiedensohler A (1996) Overview of the atmospheric research program during the International Ocean Expedition of 1991 (IAOE-1991) and its scientific results. Tellus 48B:136–155

Leck C, Nilsson ED, Bigg EK, Bcklin L (2001) The atmospheric program of the Arctic Ocean Expedition 1996 (AOE-1996) - an overview of scientific objectives, experimental approaches and instruments. J Geophys Res 106(D23):32051–32067

Leck C, Tjernström M, Matrai P, Swietlicki E, Bigg K (2004) Can marine micro-organisms influence melting of the Arctic pack ice? EOS 85:25–36

Lindsay RW, Zhang J (2005) The thinning of Arctic sea ice, 1988–2003: have we passed a tipping point? J Clim 18:4879–4894

Lindsay RW, Zhang J, Schweiger A, Steele M, Stern H (2009) AArctic sea ice retreat in 2007 follows thinning trend. J Clim 22:165–176

Liou KN (1992) Radiation and cloud processes in the atmosphere, Oxford monographs on geology and geophysics no. 20. Oxford University Press, Oxford, p. 487

Liou KN, Fu Q, Ackerman TP (1988) A simple formulation of the delta-four-stream approximation for radiative transfer parameterizations. J Atmos Sci 45:1940–1947

Liu Y, Key JR, Wang X (2008) The influence of changes in cloud cover on recent surface temperature trends in the Arctic. J Clim 21:705–715

Markus T, Stroeve JC, Miller J (2009) Recent changes in Arctic sea ice melt onset, freezeup, and melt season length. J Geophys Res 114. doi:10.1029/2009JC005436

McPhee MG (2008) Air–ice–ocean interaction: turbulent boundary layer exchange processes. Springer, Berlin

Moran KP, Martnew BE, Post MJ, Kropfli RA, Welsh DC, Widener KB (1998) An unattended cloud-profiling radar for use in climate research. Bull Am Meteorol Soc 79:443–455

Nicolaus M, Hudson SR, Gerland S, Munderloh K (2010) A modern concept for autonomous and continuous measurements of spectral albedo and transmittance of sea ice. Cold Regions Sci Technol 62:14–28

Nilsson ED, Rannik U, Hakansson M (2001) Surface energy budget over the central Arctic Ocean during late summer and early freeze-up. J Geophys Res 106(D23):32187–32205

Overland JE (2009) The case for global warming in the Arctic. In: Nihoul JCJ, Kostianoy AG (eds) Influence of climate change on the changing Arctic and Sub-Arctic conditions. Springer, Dordrecht, pp. 13–23

Overland JE, Turner J, Francis J, Gillett N, Marshall G, Tjernström M (2008) The Arctic and Antarctic: two faces of climate change. EOS 89:177–184

Perovich DK (2005) The aggregate-scale portioning of solar radiation in Arctic sea ice during the Surface Heat Budget of the Arctic Ocean (SHEBA) field experiment. J Geophys Res 110(C03002):1–12. doi:10.1029/2004JC002512

Perovich DK, Richter-Menge JA, Jones KF, Light B (2008) Sunlight, water, and ice: extreme Arctic sea ice melt during the summer of 2007. Geophys Res Lett 35:L11501. doi:10.1029/2008GL034007

Persson POG, Fairall CW, Andreas EL, Guest PS, Perovich DK (2002) Measurements near the Atmospheric Surface Flux Group tower at SHEBA: Near-surface conditions and surface energy budget. J Geophys Res 107(8045):1–21. doi:10.1029/2000JC000705

Polyakov I, Timokhov L, Hansen E, Piechura J, Walczowski W, Ivanov V, Simmons H, Fahrbach E, Hölemann J, Steele M, Pickart R, Fortier L, Schauer U, Beszczynska-Möller A, Holliday NP, Dmitrenko I, Dickson R, Gascard JC, Mauritzen C (2007) Observational program tracks Arctic Ocean transition to a warmer state. EOS Trans 88:398. doi:10.1029/2007EO400002

Ramanathan V, Cess RD, Harrison EF, Minnis P, Barkstrom BR, Ahmad E, Hartman D (1989) Cloud-radiative forcing and climate: results for the Earth Radiation Budget Experiment. Science 243:57–63

Rigor IG, Colony RL, Martin S (2000) Variations in surface air temperature observations in the Arctic 1979–1997. J Clim 13:896–914

Roebber PJ, Bruening SL, Schultz DM, Cortinas JV Jr. (2003) Improving snowfall forecasting by diagnosing snow density. Weather Forecast 18:264–287

Ruffieux D, Persson POG, Fairall CW, Wolfe DE (1995) Ice pack and lead surface energy budgets during LEADEX 1992. J Geophys Res 100:4593–4612

Schneider SH (1972) Cloudiness as a global climate feedback mechanism: the effects on the radiation balance and surface temperature variations in cloudiness. J Atmos Sci 29:1413–1422

Serreze MC, Holland MM, Stroeve J (2007) Perspectives on the Arctic's shrinking sea-ice cover. Science 315:1533–1536. doi: 10.1126/science.1139426

Shimada Kea (2006) Pacific Ocean inflow: Influence on catastrophic reduction of sea ice cover in the Arctic Ocean. Geophys Res Let 33:L08605. doi:10.1029/2005GL025624

Shupe MD, Intrieri JM (2004) Cloud radiative forcing of the Arctic surface: the influence of cloud properties, surface albedo, and solar zenith angle. J Clim 17:616–628

Sirevaag A, Fer I (2009) Early spring oceanic heat fluxes and mixing observed from drift stations North of Svalbard. J Phys Oceanogr 39(12):3049–3069. doi:10.1175/2009jpo4172.1

Stephens GL (1978) Radiation profiles in extended water clouds. II. Parameterization schemes. J Atmos Sci 35:2123–2132

Tjernström M, Leck C, Persson POG, Jensen ML, Oncley SP, Targino A (2004) The summertime Arctic atmosphere: meteorological measurements during the Arctic Ocean Experiment (AOE-2001). Bull Am Meteorol Soc 85:1305–1321

Tjernström M, Zagar M, Svensson G, Cassano JJ, Pfeifer S, Rinke A, Wyser K, Dethloff K, Jones C, Semmler T, Shaw M (2005) Bull Am Meteorol Soc. Boundary Layer Meteorol 117:337–381. doi: 10.1007/s10546-004-7954-z

Walsh JE, Chapman WL (1998) Arctic cloud-radiation-temperature associations in observational data and atmospheric reanalyses. J Clim 11:3030–3045

Westwater ER, Han Y, Shupe MD, Matrosov SY (2001) Analysis of integrated cloud liquid and precipitable water vapor retrievals from microwave radiometers during SHEBA. J Geophys Res 106:32,019–32,030

Wilczak JM, Oncley SP, Stage SA (2001) Sonic anemometer tilt correction algorithms. Boundary Layer Meteorol 99:127–150

Zeng J, Matsunaga T, Mukai H (2008) METEX: a flexible tool for air trajectory calculation. Environ Model Software 25:607–608

Zhang T, Stamnes K, Bowling SA (2001) Impact of the atmospheric thickness on the atmospheric downwelling longwave radiation and snowmelt under clear-sky conditions in the Arctic and Subarctic. J Clim 14:920–939

Zhang J, Lindsay R, Steele M, Schweiger A (2008a) What drove the dramatic retreat of arctic sea ice during summer 2007? Geophys Res Lett 35:L11505. doi:10.1029/2008GL034005

Zhang X, Sorteberg A, Zhang J, Gerdes R, Comiso JC (2008b) Recent radical shifts of atmospheric circulations and rapid changes in Arctic climate system. Geophys Res Lett 35:L22701. doi: 10.1029/2008GL035607